Characterization of mode II delamination behaviour of poplar plywood and LVL

H. Hadiji, J. Serra, R. Curti, D. Gebrehiwot, Bruno Castanié

Journal Pre-proofs

Characterization of mode II delamination behaviour of poplar plywood and LVL

H. Hadiji, J. Serra, R. Curti, D. Gebrehiwot, B. Castanié

PII: S0167-8442(24)00103-4
DOI: https://doi.org/10.1016/j.tafmec.2024.104354
Reference: TAFMEC 104354

To appear in: *Theoretical and Applied Fracture Mechanics*

Received Date: 29 September 2023
Revised Date: 5 January 2024
Accepted Date: 27 February 2024

Please cite this article as: H. Hadiji, J. Serra, R. Curti, D. Gebrehiwot, B. Castanié, Characterization of mode II delamination behaviour of poplar plywood and LVL, *Theoretical and Applied Fracture Mechanics* (2024), doi: https://doi.org/10.1016/j.tafmec.2024.104354

Characterization of mode II delamination behaviour of poplar plywood and LVL

H. Hadiji[1], J. Serra[1*], R. Curti[1], D. Gebrehiwot[1], B. Castanié[1]

[1] Institut Clément Ader (ICA), Université de Toulouse, CNRS UMR 5312, ISAE-SUPAERO, INSA, IMT Mines Albi, UPS, Toulouse, France.

*corresponding author: joel.serra@isae-supaero.fr

Abstract

The aim of this work was to characterize the interlaminar fracture toughness of poplar laminate veneer lumbers (LVL) under mode II loading. To this end, the Four-point End Notched Flexure test (4ENF) was chosen, and crack propagation was continuously monitored during the test using a stereo-correlation set-up. The R-curve was then obtained by a compliance calibration method, expressing the evolution of the critical strain energy release rate as a function of the crack length for the tested specimens. Two different interfaces were investigated, with the interfacial fibre orientations of 0°/90° and 0°/0°. The results show that the interlaminar fracture toughnesses are about 2.2 and 2.5 kJ/m^2 for interfaces 0°/0° and 0°/90°, respectively. These values are higher than those of carbon-epoxy laminates. Fracture surface morphologies were analysed to understand the effect of fibre orientation on the fracture toughness. Finally, the fracture toughness was calculated with a compliance-based beam method, and good agreement was found between the two methods.

Keywords

Mode II, interlaminar fracture toughness, plywood, 4ENF, R-curve.

Nomenclature

The symbols used throughout this document are summarized in the list below.

l	specimen length
b	specimen width
h	specimen thickness
L	half distance between the two outer rollers
P	load applied to the specimen
δ	vertical displacement of the specimen
a	crack length
a_0	initial crack length
C	compliance
C_0	initial compliance
G_{IIc}	critical strain energy release rate in mode II
G_{Ic}	critical strain energy release rate in mode I
E_L	Young's modulus in the longitudinal direction
I	moment of inertia of the crack-free portion in a 4ENF specimen
X	specimen length direction
Z	specimen thickness direction

1. Introduction

Wood and its composites have repeatedly proven their mechanical performance in many aeronautic and automotive applications [1–6]. The De Havilland Mosquito is a successful example of wood's performance in aircraft [1,2]. This aeroplane, designed with a wood sandwich structure during the Second World War, made its first flight in 1940 at a speed of up to 612 *km/h*. It was one of the best aircraft of the Second World War, distinguished by its extraordinary missions and excellent mechanical performance. Wood has also been used extensively in the automotive industry, e.g. in the "Costin Nathan" racing car, which competed in the Le Mans 24-hour race in France in 1967 [4]. Its designer, the English engineer Franck Costin, chose plywood for the chassis of his car to make it lighter, achieving a weight of only 450 *kg*.

Wood's historically proven performance, lightness and bio-source make it a potential material for use in structural components. Therefore, quantifying the fracture toughness of wood and wood veneer panels, such as laminated veneer lumbers (LVL) and plywood, is crucial if their damage and failure behaviour is to be understood. In particular, the fracture toughness under mode II loading, which can be a recurrent loading mode in structural applications, needs to be better known.

Several test methods are available for experimentally characterizing mode II interlaminar fracture toughness [7–9]. The End Notched Flexure (ENF) test, standardized as ASTM international standard D7905/D7905M-14 for composite materials, is the most widely used [10]. In this test, the specimen, pre-cracked at the interface to be characterized, is positioned on a 3-point bend fixture. The test is easy to perform, but the crack propagation is only stable when the ratio between the initial crack length and the specimen's mid span length is higher than 0.7. This condition is reduced for the End Load Split test (ELS), standardized as ISO 15 114 [11]. In this test, the specimen is clamped on one side and loaded on the other, and the ratio between initial crack length and the specimen's mid span must be higher than 0.55, to obtain stable crack propagation. Although the stability condition is reduced compared to the ENF test, the set-up for an ELS test is much more complicated. To overcome test instability issues, two test configurations are proposed in the literature. The first one is the Tapered End-Notched Flexure test (TENF) [12,13], where the stability is given by the adopted tapered design of the sample. The second test is the Four point End Notched Flexure test (4ENF) proposed by Martin and Davidson [14] in 1999. In a 4ENF test, the pre-cracked specimen is positioned on two support points and the load is applied by two loading points. This test is not standardized, but its advantage is that it always ensures a stable crack propagation without any conditions being imposed for the specimen dimensions or shape.

Several studies have characterized the mode II delamination behaviour of solid wood. For example, Yoshihara and Ohta [15,16] studied the mode II fracture toughness of Sitka Spruce with ENF tests. Because of the crack propagation stability limits of the ENF test, the 4ENF test was adopted by Yoshihara in recent works on the same material [17,18]. As mode II is an in-plane delamination mode, there is no opening of the specimen. So, there is no clear visibility of the crack tip as it propagates and measuring the crack length is therefore very complicated. For this reason, Yoshihara has carried out 4ENF testing under a magnifying glass placed in front of a specimen having pre-drawn lines on its crack-free region. Once the load is applied and the initial crack is observed to reach a pre-drawn line, the specimen is unloaded and then reloaded until the crack reaches the next line. Consequently, several load-unload cycles are needed which make the test lasts for 90 minutes. De Moura et al.[19] have also worked on solid wood by quantifying the mode II delamination of Pinus pinaster wood specimens. To overcome the

difficulty of crack monitoring during the test, the authors propose to calculate an equivalent crack length based on the beam theory, the load-displacement data, and the Young's modulus of the specimen. An R-curve describing the evolution of the critical strain energy release rate with the equivalent crack length was then obtained. Using Digital Image Correlation to monitor the crack length, Rahman et al. [20] have evaluated the fracture toughness of solid and glued sawn timber with ENF tests. In fact, they have placed digital vertical line probes at every millimetre length along the initial crack. Each line consists of two-point probe on either side of the crack. When there is sliding between the two parts of the specimen, the coordinates of the two-point probes change which permits to calculate the horizontal extension and therefore the crack length.

Although many studies have focused on determining the fracture toughness of solid wood, very few have studied that of LVL or plywood. Xiao et al. [21] have quantified the mode II fracture toughness of poplar LVL by using compact tensile test. This test enabled them to determine only one value of fracture toughness corresponding to the propagation of the pre-crack. Nevertheless, this result does not provide sufficient data to plot an R-curve or to understand the delamination behaviour at different crack lengths. Interested in plywood failure behaviour, El Moustaphaoui et al. [22–24] have characterized the mode I and II, and mixed mode fracture toughness of the interface between two plies in the direction of Ceiba wood fibres (0° direction). For mode II in particular, El Moustaphaoui et al. [22–24] chose the ELS test for their Ceiba plywood specimens. To find the R-curve without needing to monitor the crack length experimentally, they referred to the beam theory using the load and displacement from ELS test data and the longitudinal Young's modulus from tensile tests. They concluded that the energy required for delamination under mode II loading was higher than that for mode I or mixed mode. By investigating fracture surfaces of the specimens after failure, El Moustaphaoui et al. [22–24] highlighted the significant presence of fibre bridging for mode I and mixed mode but noted that those phenomena were absent for ELS specimens under mode II loading.

In all the works cited above, the mode II interlaminar fracture toughness was found by considering a 0°/0° interface only, and without continuous crack tracking as the crack propagates during the test. Nevertheless, real-time monitoring of the crack propagation is essential to analyse the delamination path locally and to filter out any fracture toughness corresponding to a non-interfacial delamination. Also, LVL and plywood are, by definition, composed of parallel veneers and cross-ply veneers perpendicular to one another, respectively. So, it is important to determine the mode II fracture toughness of LVL or plywood not only with 0°/0° but mostly 0°/90° interfaces.

In this context, the work presented here proposes a characterization of the mode II interlaminar fracture toughness of poplar plywood with 0°/0° and 0°/90° interfaces. The 4ENF test was chosen for this work since it ensures stable crack propagation and does not impose any constraints on the specimen dimensions. Also, continuous monitoring of crack propagation was performed during the test and a stereo correlation method is proposed to calculate the crack length and to locally analyse the delamination path of the crack as it propagates. Two data reduction methods are then detailed to obtain the R-curves. The results obtained are explained by in-situ observations of the fracture surface interfaces.

2. Materials and manufacturing

Poplar plywood plates were manufactured by pressing glued poplar veneers for 5 hours at 10 bars and 25 °C. The poplar veneers, with a thickness of 1 mm and a mean density of 348 kg/m^3, were supplied by the LaBoMaP laboratory in Cluny, France. The moisture content of the wood

was about 10%. A polyurethane-based glue, commercialized as Kleiberit PUR 510 FIBERBOND, was used at a rate of 250 *g/m²* between all plies. Two poplar plywood plates were manufactured as depicted in Figure 1: one plate with a 0°/0° interface and a second plate with a 0°/90° interface. The aim of considering 0°/0° and 0°/90° interfaces is to consider the two possible paths of a cack propagation in LVL and plywood materials. In fact, LVL is made from glued veneers parallel to one another. Plywood, on the other hand, is made from cross-ply veneers perpendicular to one another. So, a crack in LVL or plywood can propagate through 0°/0° or 0°/90° interfaces. It is therefore necessary to test specimens with a 0°/0° as well as a 0°/90° interface to understand its influence on the mode II fracture toughness. For the first manufactured plate, 8 plies $[0°_8]$, oriented at 0° were stacked and pressed. For the second plate, 13 plies $[0°_6, 90°, 0°_6]$, were used: 12 plies oriented at 0° and 1 perpendicular ply (90° ply) placed at one side of the pre-cracked interface. The number of plies was chosen after preliminary tests on 0°/0° and 0°/90° specimens with 8 plies $[0°]_8$ and 9 plies $[0°_4, 90°, 0°_4]$, respectively, which were available from a previous mode I test campaign [25]. With these preliminary tests, bending failure occurred before crack propagation for the 0°/90° specimens. For this reason, the choice was made to increase the stiffness of the 0°/90° specimens by increasing the number of plies along the thickness for the work presented. Thirteen specimens with 0°/0° interface and 15 specimens with 0°/90° interface were cut from the plates, with the dimensions *(l, b, h)* of $250 \times 25 \times 8\ mm^3$ and $250 \times 25 \times 13\ mm^3$, respectively. It is noteworthy that, to create the pre-crack a_0 (shown in Figure 1), a Teflon film was placed between the two surfaces of the interface to be characterized, over a length of 40 mm, during the manufacturing process. Then, the initial crack on each specimen was extended with a cutter blade to eliminate any possible glue concentration at the end of the Teflon film.

3. Experimental procedure

3.1.Test set-up

The 4ENF test was chosen to characterize the mode II interlaminar fracture toughness of the studied poplar plywood specimens. The notched specimen was positioned at two support points (outer rollers) and the load was applied at two other points (inner rollers). The distances between the four rollers (Figure 2) were chosen to be symmetrical with the central vertical axis of the machine and to have a large distance between the two inner rollers, which was sufficient for large crack propagation. The diameter of the rollers was about 10 mm to ensure a sufficient contact surface with the specimen.

Figure 3 shows the test set-up used. The 4ENF test apparatus was fixed on an Instron 5900 universal test machine equipped with a 10 kN force cell and the test was performed under an imposed displacement speed of 2 mm/min, and at ambient temperature and humidity (23.5 °C and 47% RH). The pivot connection between the machine load axis and the two inner points ensured that forces were equally distributed at both points. Therefore, the crack propagation was stable between the two inner rollers. For this reason, the specimen was positioned in such a way that the initial crack went beyond the first loading roller on the left (Figure 2), placing it in the zone of a stable crack propagation. To avoid local crushing of the wood under the rollers, silicone rubbers were used at the contact surfaces between the specimen and the four rollers. A stereo correlation device was installed in front of the specimen to monitor the test continuously. It is worth noting that this choice to carry out continuous propagation tests, which means that the load is continuously applied from the pre-crack until the specimen failure, without need to load/unload cycles permit to avoid generating residual stress effects for 0°/0° or 0°/90° specimens. The stereo correlation device consisted of two cameras with a resolution of 8 Mega

pixels each, and two light sources, as shown in Figure 3. The first camera was placed in front of the test specimen section to record the in-plane movements. The second was placed at an inclined angle to detect movements in the out-of-plane direction. This allowed the quality of the test set-up to be checked and ensured that no out-of-plane displacement occurred. One image was taken per second to record all eventual specimen deformation during the test. The advantage of the stereo correlation technique was that it provided real-time monitoring of the test. By means of the images recorded during the test, it was possible to see the delamination path clearly and to locally analyse the crack tip in each image, which corresponded to a crack propagation at the interface. This local analysis permitted any ply jumping phenomena to be detected and thus enabled the corresponding fracture toughness values to be eliminated. Hence, the fracture toughness values could be filtered to keep only those corresponding to a pure interfacial delamination. It is worth noting that the specimens were painted with white paint in a first step and sprayed with black speckles in a second step, on the thickness section that was tracked by the camera. The area of one speckle was approximately 0.014 mm^2, corresponding to a minimum size of 3 pixels, as recommended by Reu [26]. An infrared thermography camera (M3K – Telops) was also used to detect any energy-consuming movement of the specimen during the crack propagation. However, no data from the infrared camera was exploited because of the very low energy levels of the specimens. In fact, the energy released by the plywood specimens during the crack propagation was too low to be detected by the camera. Nevertheless, it was possible to identify the fibre breakage energies that indicated specimen failure, signifying the end of the exploitable part of the test.

3.2.Test method (DIC)

To calculate the interlaminar fracture toughness of the poplar plywood specimens, many inputs were needed, such as the applied load, the displacement, and the crack length.

The applied Load (P) was directly recorded during the 4ENF test via the data acquisition system of the test machine, which was synchronized with the image acquisition frequency of the camera.

For the specimen displacement and the crack length, Digital Image Correlation (DIC) was applied to each recorded image using VIC-3D® software. The software considers the first taken image (at the beginning of the test) as a reference image. On this image, a calculation zone is defined (purple zone in Figure 4) and then divided into rectangular subsets, where each subset contains 3 to 4 speckles. Any displacement of the specimen, i.e., movement of the speckles, encountered in subsequent images (during the test) are calculated using the offset, in pixels, of the speckles from the reference image.

The displacement given by the machine was that of its vertical axis, which corresponded to the displacement of the specimen and the silicone rubbers and was also affected by the set-up and the tensile machine clearances. For this reason, it was not appropriate to describe the displacement of the specimen at the support points. To find the displacement of the specimen, DIC measurements were more relevant. Four rectangular zones of interest were defined on the calculation zone of the reference image. The four rectangular zones, as shown in Figure 4, are

defined near to the four rollers: up and down rectangles on the left part of the specimen, named R_{UL} and R_{DL}, respectively, and up and down rectangles on the right side of the specimen, named R_{UR} and R_{DR}, respectively. Then, the displacements next to the rollers, corresponding to the mean displacement δ of each rectangular calculation zone, can be computed. Eventually, the relative displacement of the specimen, which is the average displacement between the left and the right side of the specimen can be calculated by the following equation:

$$\delta = \frac{\delta_r + \delta_l}{2} = \frac{(\delta_{UR} - \delta_{DR}) + (\delta_{UL} - \delta_{DL})}{2} \quad (1)$$

The crack length was calculated based on observation of a parameter called "sigma" in the VIC-3D® software. This parameter is defined as the correlation error between each image of the test and the reference image. The farther the crack propagates in a correlation zone, the larger is the difference between the two images that is not due to the deformation of the specimen. This results in a higher correlation error. First, the noise in the study area of the reference image is removed by eliminating the small values of sigma. This provides a clearer display of the crack bottom after each propagation, which corresponds to high values of sigma (crack tip in red), as depicted in Figure 5. To extract the crack tip coordinates in millimetres, a Python script relying on manual point-by-point tracking was used. For each image, three points were tracked to calculate the crack length. The first point was the origin of the crack (x_0,z_0), the second was that of the crack tip (x_f,z_f), and the third point was located between the two points, (x_1,z_1). Next, a second-order interpolation was carried out between the three points to consider the specimen curvature. Thereafter, the crack length, a, was calculated by integrating the second-order fitting function, $f(x)$, obtained between the origin and the end of the crack for each image:

$$a = \int_{x_0}^{x_f} \sqrt{1 + f'(x)^2}\,dx \quad (2)$$

4. Data reduction methods

In this section, the two methods used to find the evolution of the fracture toughness with the crack length are detailed, based on the test machine data and either the DIC procedure or the beam theory.

4.1.CCM : Compliance Calibration Method

This method is based on the test machine data and the DIC procedure. First, the specimen compliance at each crack propagation was calculated as defined in Equation 3:

$$C = \frac{\delta}{P} \quad (3)$$

Where δ is obtained from the DIC calculations described in section 3.2, and P is the load given by the test machine cell load.

The CCM method is based on the definition of a relationship between the specimen compliance and the crack length. Using the calculated compliances from Equation 3 and the evaluated crack lengths, via DIC procedure as described in section 3.2, the points describing the evolution of the compliance as respect to the crack length can be plotted, such as the specimen example depicted in Figure 6. In

the case of 4ENF test, *C=f(a)* is a linear function [17]. To find this function, the evolution of the compliance with the crack length (Figure 6) is fitted with a first order equation as follows:

$$C(a) = C_0 + C_1 a \quad (4)$$

Where C_0 and C_1 are therefore obtained from the equation of the linear fitting curve such as shown in Figure 6.

Then, the critical strain energy release rate can be calculated from the Irwin-Kies equation [27]:

$$G_{IIc} = \frac{P^2 dC}{2bda} \quad (5)$$

where *P* is the applied load, provided by the test machine, and *b* corresponds to the specimen's width, measured for each specimen.

Considering the linear distribution of the Compliance/crack length function of Equation 4, G_{IIc} can be calculated as follows:

$$G_{IIc} = \frac{C_1 P^2}{2b} \quad (6)$$

where C_1 corresponds to the slope of the curve *C=f(a)*, found from the fitting equation (Eq. 4).

Thereafter, the R-curve, which describes the evolution of the calculated critical strain energy release rate at each crack propagation as a function of the corresponding crack length, can be plotted for each specimen. Figure 7 depicts an example of the R-curve obtained by Compliance Calibration Method.

4.2.CBBM: Compliance Based Beam Calibration Method

As its name indicates, the Compliance Based Beam Method uses beam theory to calculate the compliance for each crack length. To this end, the displacement equation at the two loading points determined by Martin and Davidson [14] is modified according to the dimensions of the 4ENF test set-up and the size of the specimens of this work. The displacement expression is then used to find the following Compliance expression:

$$C_{theo} = \left(\frac{23L^3}{1944.E_L I} + \frac{25L^2}{1944.E_L I}\right) + \frac{L^2}{12.E_L I}.a \quad (7)$$

By combining Equation 5 and Equation 7, the critical strain energy release rate becomes:

$$G_{IIc} = \frac{P^2 L^2}{24bE_L I} \quad (8)$$

The Young's modulus in Equation 8 is a parameter that can show significant variability from one specimen to another for a natural material such as wood. For this reason, it is more accurate to know the specific Young's modulus of each specimen tested. In this context, De Moura et al. [19] suggested using the initial compliance corresponding to the initial crack, a_0, to find Young's modulus for each specimen. This approach is adopted in this study, and the effective Young's modulus of each specimen is calculated from the following equation:

$$C_0 = \left(\frac{23L^3}{1944.E_L I} + \frac{25L^2}{1944.E_L I}\right) + \frac{L^2}{12.E_L I}.a_0 \quad (9)$$

Young's modulus can be therefore calculated as follows:

$$E_L = \frac{23L^3+25L^2}{1944.I.C_0} + \frac{L^2}{12.I.C_0}.a_0 \quad (10)$$

By replacing the Young's modulus obtained from Equation 10 in Equation 8, the critical strain energy release rate can be therefore calculated and the R-curve from the CBBM method can be plotted, as depicted in Figure 7.

5. Results and discussion

5.1. Load-displacement responses

Figure 8 shows all the force-displacement curves for the seven 0°/0° and the ten 0°/90° specimens that were chosen. In fact, for the other tested specimens, the data were unexploitable because the fracture has occurred near to the first loading roller, before any crack propagation. For both 0°/0° and 0°/90° specimens, the curves show three different regions. First, the curve starts with a linear behaviour of force versus displacement up to an imposed displacement of 1.6 mm for 0°/0° and 1.4 mm for 0°/90° on average. In this linear part, the slope is constant, and no delamination is observed. Second, non-linear behaviour begins when the force reaches a critical value, corresponding to the beginning of delamination. This is reflected by a change in the slope of the force/displacement curve, which consequently corresponds to a crack propagation. In fact, the decreasing slopes of the force/displacement curve corresponds to different compliances and corresponding crack propagation. During this propagation, the force is slightly increased in the 0°/0° case and is practically constant for 0°/90°, which is to be expected with a 4ENF test that promises stable crack propagation [14]. Eventually, the curve shows a drastic drop in the value of the force, corresponding to total specimen failure.

5.2. Crack length measurements

As mentioned in section 3.2, the DIC technique is used to locate the position of the crack tip and subsequently to calculate the corresponding crack length. The aim of this section is to check the accuracy of the final crack length calculated by the DIC method against the real measurement from the specimen under test. To this end, the final crack length was measured with digital vernier callipers on the specimen after the test. In fact, a light spot is placed in front of the section of the tested specimen. The presence of black and white speckles on this section and the use of a magnifying glass help to visualize the crack more clearly and find its tip, and then, measure the crack length. Although this method is not very accurate, it does give an order of magnitude of the real final crack length, so that it can be compared with that obtained via DIC procedure. It is worth noting that this measurement was made only for specimens that had not shown any failure in the crack propagation zone, because these failures prevent from clearly identifying the crack tip. Table 1 summarizes the final crack length measured for five specimens, compared to that calculated via the DIC method. Thus, the accuracy of DIC method is determined and is found to be acceptable. In fact, the calculation of crack length with the DIC method can be achieved with less than 2% of relative difference from the actual measured values, which can be considered as negligible.

Table 1. Comparison of final crack lengths obtained from specimen measurement and DIC method.

Specimen	a_f *(mm)* From specimen measures	a_f *(mm)* From DIC technique	Relative difference (%)
0-0-2	52.80	52.71	0.17
0-0-4	55.50	56.28	-1.40
0-0-6	57.05	56.51	0.94
0-90-3	65.50	64.42	1.65
0-90-9	58.04	57.71	0.57

5.3. R curves

From the force/displacement curves, the compliance can be calculated according to Equation 3. Then, CCM and CBBM, described in Section 4, are adopted to calculate the critical strain energy release rate for each crack propagation and to obtain the R-curves. Figure 9 shows the R-curves obtained by CCM for example. As it can be seen in Figure 9, the critical strain energy release rate continuously increases as a function of the crack length until the end of the R-curve. In fact, for most of the obtained R-curves, there is no plateau portion where the critical strain energy is constant. This may be explained by the early failure of the specimens that did not allow a large crack propagation up to a steady state zone. The gradually upward trend of the critical strain energy release rate can be explained by the fact that, the contact surface on the crack interface increases and therefore the energy dissipated through friction increases. The absence of a plateau portion in the R-curve has also been observed for other types of wood materials in the literature [20,29]. Since no plateau portion was found in most R-curves of this study, we characterize the critical strain energy release rate by two values obtained from the R-curves: G_{II0} and G_{IIc}. G_{II0} is the critical strain energy release rate corresponding to the propagation of the initial crack a_0. Table 2 depicts G_{II0} values for all the tested specimens. As for G_{IIc}, it is obtained by averaging the critical strain energy release rate over all the crack propagation in the R-curve. The results of G_{IIc} values for 0°/0° and 0°/90° interfaces are presented in Table 3 and Table 4, respectively.

Table 2. Initial critical strain energy release rates of 0°/0° and 0°/90 specimens calculated with CCM.

Specimen 0°/0°	G_{II0} *(kJ/m²)*	Specimen 0°/90°	G_{II0} *(kJ/m²)*
0-0-1	1.19	0-90-1	2.22
0-0-2	1.05	0-90-2	1.60
0-0-3	1.89	0-90-3	1.55
0-0-4	1.77	0-90-4	2.04
0-0-5	1.35	0-90-5	1.97
0-0-6	1.55	0-90-6	1.55
0-0-7	1.49	0-90-7	2.16
		0-90-8	1.76
		0-90-9	1.83
		0-90-10	2.43
Average *(KJ/m²)*	1.47	Average (KJ/m²)	1.92
Co V. (%)	18	Co V. (%)	14

For the 0°/0° interface, the critical strain energy release rate increases with the crack propagation. Indeed, the crack begins to propagate from the initial crack. Then, it continues to propagate in a smooth and stable manner until the final crack. During this propagation, G_{IIc} increases from 1.47 to 2.77 *kJ/m²* on average (an increase of about 88%) for an average of 13 mm of stable crack propagation. From all the 0°/0° specimens tested, an average G_{IIc}value of

2.21 kJ/m^2 is obtained. It should be noted that this value is calculated from the average G_{IIc} values of all the 0°/0° specimens tested, summarized in Table 3. It can be concluded that the test has good repeatability. In fact, the coefficient of variation between G_{IIc} values is about 16.19%, which is not surprising given the well-known variability of the mechanical properties of wood from one specimen to another.

Table 3. Mean critical strain energy release rates of 0°/0° specimens.

Specimen	CCM G_{IIc} (kJ/m^2)	CBBM G_{IIc} (kJ/m^2)	Relative difference (%)
0-0-1	2.02	1.52	24
0-0-2	1.71	1.29	24
0-0-3	2.31	1.33	42
0-0-4	2.60	2.10	19
0-0-5	1.85	1.14	38
0-0-6	2.37	1.68	29
0-0-7	2.62	1.80	31
Average (KJ/m^2)	2.21	1.55	
Co V. (%)	15	19	

For the 0°/90° interface, the R-curves show the same behaviour as the 0°/0° specimens, i.e. G_{IIc} increases as the crack propagates, with an average value of 2.50 kJ/m^2 (Table 4). However, the trend of increasing in G_{IIc} from the initial to the final crack length is less remarkable than for the 0°/0° interface; during the propagation, G_{IIc} increases from 1.92 to 2.98 kJ/m^2 in an average of 28 mm of stable crack propagation. This represents an increase in G_{IIc} of 55%, i.e., a lower increase than for the 0°/0°interface. This less remarkable increase reflects greater and smoother propagation for the 0°/90° interface. One of the effects that can induce an increase of G_{IIc} is the friction between the two interface surfaces [28,29]. Indeed, as the crack propagates, the contact

surface at the interface increases, so friction becomes greater, which may require more energy to continue propagating the crack.

Table 4. Mean critical strain energy release rates of 0°/90° specimens.

Specimen	CCM G_{IIc} (kJ/m²)	CBBM G_{IIc} (kJ/m²)	Relative difference (%)
0-90-1	3.01	2.79	7
0-90-2	2.30	1.92	16
0-90-3	2.10	2.61	-24
0-90-4	2.29	2.09	8
0-90-5	1.92	2.68	-39
0-90-6	2.89	3.37	-16
0-90-7	3.46	2.70	21
0-90-8	2.06	2.11	-2
0-90-9	2.09	2.38	-13
0-90-10	2.94	2.66	9
Average (KJ/m²)	2.50	2.53	
Co V. (%)	20.85	16.83	

5.4. Discussion

In this section, we first compare the interlaminar fracture toughness values obtained from the CCM and the CBBM methods. Then, an attempt is made to analyse the causes behind the differences in the fracture toughness found between 0°/0° and 0°/90° interfaces, based on images of the surfaces of the fracture interfaces. Eventually, attention is given to a comparison of the mode II fracture toughness results with those of mode I.

5.4.1. Comparison of the fracture toughness calculated with CCM and CBBM

Figure 10 shows the results of the mean critical energy release rate calculated by the two methods (detailed values are summarized in Tables 3 and 4). As it can be seen in Figure 10, a good agreement is found between Compliance Calibration and Compliance Based Beam Methods. Also, the relative difference between CCM and CBBM is more significant for the 0°/0° interface, where it is about 30% on average, compared to approximately 15% averaged over all the relative errors of 0°/90° specimens. This can be explained by the fact that the 0°/90° specimens had longer crack lengths than the 0°/0° specimens, which resulted in calculations being averaged over a longer crack propagation zone. Hence, G_{IIc}values for 0°/90° specimens were closer to the Compliance Based Beam Method than those of 0°/0° specimens.

5.4.2. Comparison of mode II delamination between 0°/0° and 0°/90° interfaces

A comparison of the R-curves (Figure 9) between the two interfaces studied reveals two major differences. First, crack length propagation is greater for specimens with a 0°/90° interface. The crack propagation length in this case is about 28 mm on average, which is more than double that of specimens with the 0°/0° interface (about 13 mm on average). Second, the mean the mean value of G_{IIc} for 0°/90° interface is about 2.5 kJ/m^2, which is ~13% higher than the mean value of G_{IIc} for 0°/0°interface.

For comparative examples, we can refer to works that have studied the effect of interface angle for composite materials [30–34]. Indeed, the increase in G_{IIc}value when the interface angle increases has been observed for example by Perreira et al. [30], who have studied mode II delamination of carbon/epoxy composites with 0/θ interfaces, and concluded that the fracture toughness increased with increasing θ value. In fact, they have found a G_{IIc} equal to 1.6 and 1.1 for 0°/90° and 0°/0° interfaces, respectively. Hiley et al. [33] and Gong et al. [34] have also found the same trend for carbon-epoxy composites with 0°/0°, 0°/45° and 0°/90° interfaces.

To better explain this difference, an analysis of the delamination growth path and the fracture surfaces of the 0°/0° and 0°/90° interfaces was carried out. Figures 11 and 12 show the delamination growth path in 0°/0° and 0°/90° interfaces, respectively. In the case of 0°/0° interface, the crack propagates along the interface between the two 0° plies without jumping into other plies. With this interface between two plies, both oriented at 0°, sliding between the plies occurs easily whereas, for the 0°/90° interface, the crack propagates strictly within the 90° ply and the delamination path is quite complex [35,36]. In fact, the crack propagates in a tortuous manner between the 90° oriented fibres of the 90° ply (Figure 13). This tortuosity creates a contact surface, between the delaminated lower and upper parts of the 90° ply, that is rougher and wider than a contact surface between two 0° plies and results in more friction and therefore more released strain energy. Also, the cross oriented ply at the interface hinders interface sliding. This complex delamination path absorbs more energy to allow further crack propagation. Moreover, the fibres of the 90° ply create toughening effects as they are perpendicular to the delamination path and can be an additional source of energy absorption. Figures 14 and 15 show the fracture surfaces for 0°/0° and 0°/90° interfaces, respectively. To obtain a better view of the fracture surfaces, the specimens were opened by hand. In the case of

0°/0° interface, the fracture surfaces were very smooth as the crack propagated in the direction of the fibres, which may have facilitated its growth. For the 0°/90° interface, the fracture interface was more complicated. The fracture propagated in the 90° ply, i.e. in a direction perpendicular to the fibres. The fracture surface was larger than the 0°/0° one with localized fibre breakage. This fibre breakage behaviour was not encountered in the 0°/0° case and it could be a major energy dissipation source during the fracture process.

All these phenomena observed for 0°/90° fracture interface can be significant sources of energy absorption. So, 0°/90° specimens require greater energy to continue delaminating perpendicular to the fibres than to 0°/0° specimens do. Consequently, G_{IIc} is higher for 0°/90° than for 0°/0° interface.

5.4.3. Mode II and mode I fracture toughnesses

As mentioned in Section 2, the mode I of poplar plywood was also studied as a part of the same project. The results showed that the G_{Ic} value was about 0.4 and 0.2 kJ/m^2 for 0°/0° and 0°/90° interfaces, respectively [25]. The G_{IIc} in mode II is therefore 5 to 12 times greater than that in mode I. This can be explained by the phenomenon of sliding delamination in mode II, which is different from the opening phenomenon of mode I and may require more energy to propagate a crack. This result agrees with literature results for solid wood, LVL or composite materials (Table 5). However, no clear trend can be drawn from the ratio between mode II and mode I fracture toughness as this ratio is very dependent on the nature of the material and the characteristics of reinforcement fibres (wood or synthetic fibres). In comparison to synthetic fibre reinforced composites, wood has a lower mode I fracture toughness. On the other hand, it can be clearly seen that the mode II fracture toughness of wood or its composites is significantly higher than those of carbon or glass reinforced composites, whence the advantage of wood as a replacement for petro-sourced composites, especially for structure components subjected to mode II loading conditions.

Table 5. Mode I and mode II fracture toughness of poplar plywood compared to wood and composite materials from the literature.

Material	$G_{Ic}(kJ/m^2)$	$G_{IIc}(kJ/m^2)$	G_{IIc}/G_{Ic}
Current study (0°/0°)	0.4	2.1	5.25
Current study (0°/90°)	0.2	2.5	12.50
Radiata pine LVL	0.67	4.01	5.96

[37]			
Radiata pine timber [37]	0.49	6.96	14.20
Pinus Pinaster [38]	0.34	2.51	7.38
Spruce massive wood [39]	0.18	0.74	4.11
Carbon/epoxy [40]	0.5	1.60	3.2
Woven E-glass /epoxy [41,42]	0.42	1.10	2.62
UD E-glass /polyester [43]	0.40	0.74	1.85

6. Conclusions

With the aim of palliating the lack of literature works on the influence of the interfacial fibre direction on mode II fracture toughness of wood and wood composites, the current work presents, for the first time, a detailed quantification of G_{IIc} considering two different interfaces: 0°/0° and 0°/90° of poplar LVL and plywood, tested under mode II loading by means of Four-point End Notched Flexure tests. The results reveal an increase in G_{IIc} for the 0°/90° interface compared to the 0°/0° interface. Analysis of the fracture interface shows different delamination paths in the two cases: a propagation of the crack at the interface between the two 0° plies (for 0°/0° interface specimens) or within the 90° ply (for 0°/90° interface specimens). Moreover, the aspect of the fracture surfaces is another important factor affecting delamination resistance. The complex crack propagation between the 90° fibres and their breakage in the 0°/90° interface, together with the high resistance of the 90° fibres, perpendicular to the delamination path, were found to be very important energy dissipation mechanisms that could explain the higher G_{IIc} for the 0°/90° interface compared to 0°/0° interface. A Compliance Based Beam Method was also deployed to calculate the fracture toughness in both cases: 0°/0° and 0°/90° interfaces, and good agreement was found with the experimental results.

This study has given a quantification of the mode II fracture toughness of poplar plywood, while investigating the effect of the increase of fibre orientation at the interface, which creates energy absorption mechanisms resulting in greater toughness. The results obtained in this study and in the previous mode I study provide fracture toughness values that can be useful to predict failure at the scale of structural components by using numerical models, such as the Discrete Ply Model (DPM) [44–47], and open up design opportunities for more damage-tolerant wood composites. The high value of mode II obtained can also explain the good impact and compression after impact behaviour of plywood [48,49].

7. Funding

This work was supported by the Swiss foundation "Lopez Loreta pour l'Excellence Académique" under the VIRTUOSE project.

References

[1] B. Castanié, A. Peignon, C. Marc, F. Eyma, A. Cantarel, J. Serra, R. Curti, H. Hadiji, L. Denaud, S. Girardon, B. Marcon, Wood and plywood as eco-materials for sustainable mobility: A review, Compos. Struct. 329 (2024) 117790. https://doi.org/10.1016/j.compstruct.2023.117790.

[2] J. Sutherland, Revival of structural timber in Britain after 1945, Constr. Hist. Soc. 25 (2010) 101–113. https://www.jstor.org/stable/41613962.

[3] A. Klemin, Aviation Surveyed, Sci. Am. 170 (1944) 214–216. https://www.jstor.org/stable/10.2307/24997774.

[4] J. Susainathan, F. Eyma, E. De Luycker, A. Cantarel, B. Castanie, Manufacturing and quasi-static bending behavior of wood-based sandwich structures, Compos. Struct. 182 (2017) 487–504. https://doi.org/10.1016/j.compstruct.2017.09.034.

[5] U. Müller, T. Jost, C. Kurzböck, A. Stadlmann, W. Wagner, S. Kirschbichler, G. Baumann, M. Pramreiter, F. Feist, Crash simulation of wood and composite wood for future automotive engineering, Wood Mater. Sci. Eng. 15 (2020) 312–324. https://doi.org/10.1080/17480272.2019.1665581.

[6] A. Elmendorf, Plywood and its uses in automobile construction, SAE Trans. 15 (1920) 863–884. https://www.jstor.org/stable/44717914.

[7] P. Davies, G.D. Sims, B.R.K. Blackman, A.J. Brunner, K. Kageyama, M. Hojo, K. Tanaka, G. Murri, C. Rousseau, B. Gieseke, R.H. Martin, Comparison of test configurations for determination of mode II interlaminar fracture toughness results from international collaborative test programme, Plast. Rubber Compos. 28 (1999) 432–437. http://dx.doi.org/%2010.1179/146580199101540600.

[8] P. Davies, B.R.K. Blackman, A.J. Brunner, Standard Test Methods for Delamination Resistance of Composite Materials: Current Status, Appl. Compos. Mater. 5 (1998) 345–364.

[9] P. Davies, Review of standard procedures for delamination resistance testing, in: Delamination Behav. Compos., Woodhead Publishing Series in Composites Science and Engineering, 2008: pp. 65–86. https://doi.org/10.1533/9781845694821.1.65.

[10] X. Liu, T. Sun, Z. Wu, H. He, Mode II interlaminar fracture toughness of unidirectional fiber-reinforced polymer matrix composites with synthetic boehmite nanosheets at room temperature and low temperature, J. Compos. Mater. 52 (2018) 945–952. https://doi.org/10.1177/0021998317716529.

[11] H. Wang, T. Vu-Khanh, Use of end-loaded-split (ELS) test to study stable fracture behaviour of composites under mode II loading, Compos. Struct. 36 (1996) 71–79. https://doi.org/10.1016/S0263-8223(96)00066-9.

[12] P. Qiao, J. Wang, J.F. Davalos, Analysis of tapered ENF specimen and characterization of bonded interface fracture under Mode-II loading, Int. J. Solids Struct. 40 (2003) 1865–1884. https://doi.org/doi:10.1016/S0020-7683(03)00031-3.

[13] J. Wang, P. Qiao, Fracture Toughness of Wood-Wood and Wood-FRP Bonded Interfaces Under Mode-II Loading, J. Compos. Mater. 37 (2003) 875–897. https://doi.org/10.1177/0021998303037010002.

[14] R.H. Martin, B.D. Davidson, Mode II fracture toughness evaluation using four point bend, end notched flexure test, Plast. Rubber Compos. 28 (1999) 401–406. https://doi.org/10.1179/146580199101540565.

[15] H. Yoshihara, M. Ohta, Measurement of mode II fracture toughness of wood by the end-notched flexure test, J. Wood Sci. 46 (2000) 273–278. https://doi.org/10.1007/BF00766216.

[16] H. Yoshihara, Resistance curve for the mode II fracture toughness of wood obtained by the end-notched flexure test under the constant loading point displacement condition, J. Wood Sci. 49 (2003) 210–215. https://doi.org/10.1007/s10086-002-0467-9.

[17] H. Yoshihara, Mode II R-curve of wood measured by 4-ENF test, Eng. Fract. Mech. 71 (2004) 2065–2077. https://doi.org/10.1016/j.engfracmech.2003.09.001.

[18] H. Yoshihara, Theoretical analysis of 4-ENF tests for mode II fracturing in wood by finite element method, Eng. Fract. Mech. 75 (2008) 290–296. https://doi.org/10.1016/j.engfracmech.2007.03.043.

[19] M.F.S.F. de Moura, M.A.L. Silva, J.J.L. Morais, N. Dourado, Mode II fracture characterization of wood using the Four-Point End-Notched Flexure (4ENF) test, Theor. Appl. Fract. Mech. 98 (2018) 23–29. https://doi.org/10.1016/j.tafmec.2018.09.008.

[20] S.A. Rahman, M. Subhani, M. Ashraf, Mode-II progressive fracture of sawn timber and timber-adhesive bond: experimental evaluation of end notched flexure (ENF) testing using DIC, Eur. J. Wood Wood Prod. 81 (2023) 1437–1453. https://doi.org/10.1007/s00107-023-01968-x.

[21] Z. Xiao, C. Li, B. Shu, S. Tang, X. Yang, Y. Liu, Experimental Study of Mode-I and Mode-II Interlaminar Fracture Characteristics of Poplar LVL, J. Renew. Mater. 11 (2023) 245–255. https://doi.org/10.32604/jrm.2023.020751.

[22] A. El Moustaphaoui, A. Chouaf, K. Kimakh, Experimental and numerical study of the delamination of Ceiba plywood under mode I, mode II and mixed-mode (I + II) loading using the

DCB, ELS and MMF tests, Int. J. Fract. 231 (2021) 1–20. https://doi.org/10.1007/s10704-021-00557-4.

[23] A. EL Moustaphaoui, A. Chouaf, M. Chergui, K. Kimakh, Modeling of macroscopic delamination of plywood using design of experiments method, J. Indian Acad. Wood Sci. 16 (2019) 144–154. https://doi.org/10.1007/s13196-019-00240-1.

[24] A. El Moustaphaoui, A. Chouaf, K. Kimakh, M. Chergui, Determination of the onset and propagation criteria of delamination of Ceiba plywood by an experimental and numerical analysis, Wood Mater. Sci. Eng. 16 (2021) 325–335. https://doi.org/10.1080/17480272.2020.1737963.

[25] A. Peignon, J. Serra, L. Gélard, A. Cantarel, F. Eyma, B. Castanié, Mode I delamination R-curve in poplar laminated veneer lumber, Theor. Appl. Fract. Mech. 126 (2023) 103982. https://doi.org/10.1016/j.tafmec.2023.103982.

[26] P. Reu, All about speckles: Speckle Size Measurement, Exp. Tech. 38 (2014) 1–2. https://doi.org/10.1111/ext.12110.

[27] G.R. Irwin, J.A. Kies, Fracturing and fracture dynamics, Weld. J. Res. Suppl. 31 (1952) 95–100.

[28] B.D. Davidson, X. Sun, Effects of Friction, Geometry, and Fixture Compliance on the Perceived Toughness from Three-and Four-Point Bend End-Notched Flexure Tests, J. Reinf. Plast. Compos. 24 (2005) 1611–1628. https://doi.org/10.1177/0731684405050402.

[29] B.D. Davidson, X. Sun, A.J. Vinciquerra, Influences of Friction, Geometric Nonlinearities, and Fixture Compliance on Experimentally Observed Toughnesses from Three and Four-point Bend End-notched Flexure Tests, J. Compos. Mater. 41 (2007) 1177–1196. https://doi.org/10.1177/0021998306067304.

[30] A.B. Pereira, A.B. de Morais, A.T. Marques, P.T. de Castro, Mode II interlaminar fracture of carbon/epoxy multidirectional laminates, Compos. Sci. Technol. 64 (2004) 1653–1659. https://doi.org/10.1016/j.compscitech.2003.12.001.

[31] M. Salamat-Talab, M.M. Shokrieh, M. Mohaghegh, On the R-curve and cohesive law of glass/epoxy end-notch flexure specimens with 0//θ interface fiber angles, Polym. Test. 93 (2021) 106992. https://doi.org/10.1016/j.polymertesting.2020.106992.

[32] M. Kharratzadeh, M.M. Shokrieh, M. Salamat-talab, Effect of interface fiber angle on the mode I delamination growth of plain woven glass fiber-reinforced composites, Theor. Appl. Fract. Mech. 98 (2018) 1–12. https://doi.org/10.1016/j.tafmec.2018.09.006.

[33] M.J. Hiley, Delamination between multi-directional ply interfaces in carbon-epoxy composites under static and fatigue loading, in: Eur. Struct. Integr. Soc., European Structural Integrity Society, 2000: pp. 61–72. https://doi.org/10.1016/S1566-1369(00)80008-4.

[34] Y. Gong, K. Xia, Y. Wang, L. Zhao, J. Zhang, N. Hu, A semi-analytical model for the mode II fracture toughness of multidirectional composite laminates, Thin-Walled Struct. 182 (2023) 110235. https://doi.org/10.1016/j.tws.2022.110235.

[35] A. Ramji, Y. Xu, M. Yasaee, M. Grasso, P. Webb, Delamination migration in CFRP laminates under mode I loading, Compos. Sci. Technol. 190 (2020) 108067. https://doi.org/10.1016/j.compscitech.2020.108067.

[36] A. Ramji, Y. Xu, M. Grasso, M. Yasaee, P. Webb, Effect of interfacial fibre orientation and PPS veil density on delamination resistance of 5HS woven CFRP laminates under mode II loading, Compos. Sci. Technol. 207 (2021) 108735. https://doi.org/10.1016/j.compscitech.2021.108735.

[37] B. Franke, P. Quenneville, Analysis of the fracture behavior of Radiata Pine timber and Laminated Veneer Lumber, Eng. Fract. Mech. 116 (2014) 1–12. http://dx.doi.org/10.1016/j.engfracmech.2013.12.004.

[38] J. Xavier, J. Morais, N. Dourado, M.F.S.F. De Moura, Measurement of Mode I and Mode II Fracture Properties of Wood-Bonded Joints, J. Adhes. Sci. Technol. 25 (2011) 2881–2895. https://doi.org/10.1163/016942411X576563.

[39] R. Putzger, P. Haller, Fracture Energy in Mode I and Mode II of Textile Reinforced Wood, in: E.E. Gdoutos (Ed.), Fract. Nano Eng. Mater. Struct., Springer Dordrecht, 2006: pp. 453–454. https://doi.org/10.1007/1-4020-4972-2_224.

[40] S. Rivallant, C. Bouvet, N. Hongkarnjanakul, Failure analysis of CFRP laminates subjected to compression after impact: FE simulation using discrete interface elements, Compos. Part Appl. Sci. Manuf. 55 (2013) 83–93. http://dx.doi.org/10.1016/j.compositesa.2013.08.003.

[41] M.R. Hosseini, F. Taheri-Behrooz, M. Salamat-talab, Mode I interlaminar fracture toughness of woven glass/epoxy composites with mat layers at delamination interface, Polym. Test. 78 (2019) 105943. https://doi.org/10.1016/j.polymertesting.2019.105943.

[42] M.R. Hosseini, F. Taheri-Behrooz, M. Salamat-talab, Mode II interlaminar fracture toughness of woven E-glass/epoxy composites in the presence of mat interleaves, Int. J. Adhes. Adhes. 98 (2020) 102523. https://doi.org/10.1016/j.ijadhadh.2019.102523.

[43] A. Szekrényes, Prestressed fracture specimen for delamination testing of composites, Int. J. Fract. 139 (2006) 213–237. https://doi.org/10.1007/s10704-006-0043-1.

[44] C. Bouvet, J. Serra, P.G. Perez, Strain rate effect of mode II interlaminar fracture toughness on the impact response of a thermoplastic PEEK composite, Compos. Part C Open Access 2 (2020) 100031. https://doi.org/10.1016/j.jcomc.2020.100031.

[45] J. Serra, A. Trellu, C. Bouvet, S. Rivallant, B. Castanié, L. Ratsifandrihana, Combined loadings after medium velocity impact on large CFRP laminated plates: Discrete ply model simulations, Compos. Part C Open Access 6 (2021) 100203. https://doi.org/10.1016/j.jcomc.2021.100203.

[46] P. Journoud, C. Bouvet, B. Castanié, F. Laurin, L. Ratsifandrihana, Experimental and numerical analysis of unfolding failure of L-shaped CFRP specimens, Compos. Struct. 232 (2020) 111563. https://doi.org/10.1016/j.compstruct.2019.111563.

[47] C. Bouvet, B. Castanié, M. Bizeul, J.-J. Barrau, Low velocity impact modelling in laminate composite panels with discrete interface elements, Int. J. Solids Struct. 46 (2009) 2809–2821. https://doi.org/10.1016/j.ijsolstr.2009.03.010.

[48] J. Susainathan, F. Eyma, E. De Luycker, A. Cantarel, B. Castanie, Experimental investigation of impact behavior of wood-based sandwich structures, Compos. Part Appl. Sci. Manuf. 109 (2018) 10–19. https://doi.org/10.1016/j.compositesa.2018.02.029.

[49] J. Susainathan, F. Eyma, E. De Luycker, A. Cantarel, C. Bouvet, B. Castanie, Experimental investigation of compression and compression after impact of wood-based sandwich

structures, Compos. Struct. 220 (2019) 236–249.
https://doi.org/10.1016/j.compstruct.2019.03.095.

Figures:

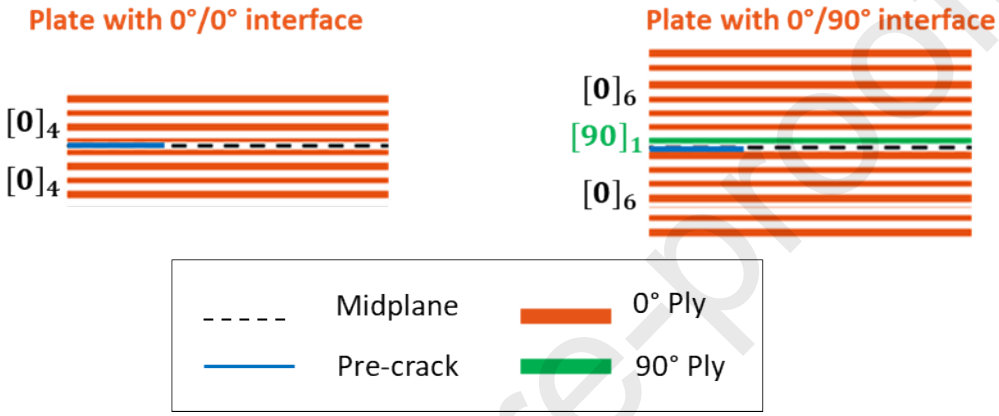

Figure 1. 0°/0° and 0°/90° specimen stacking sequences.

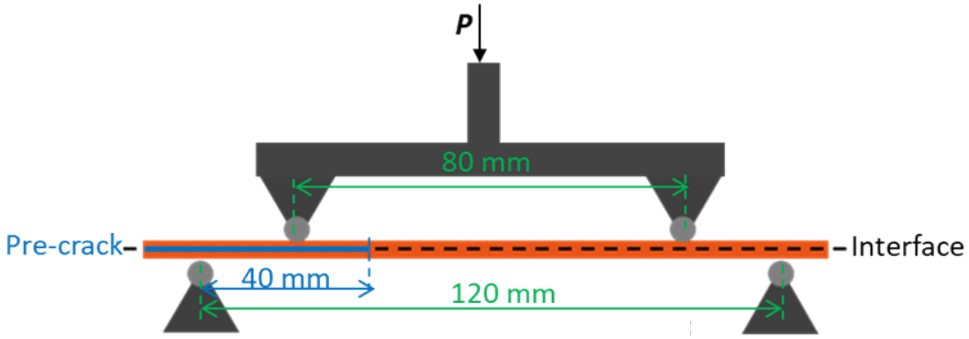

Figure 2. Geometric characteristics of the 4ENF test.

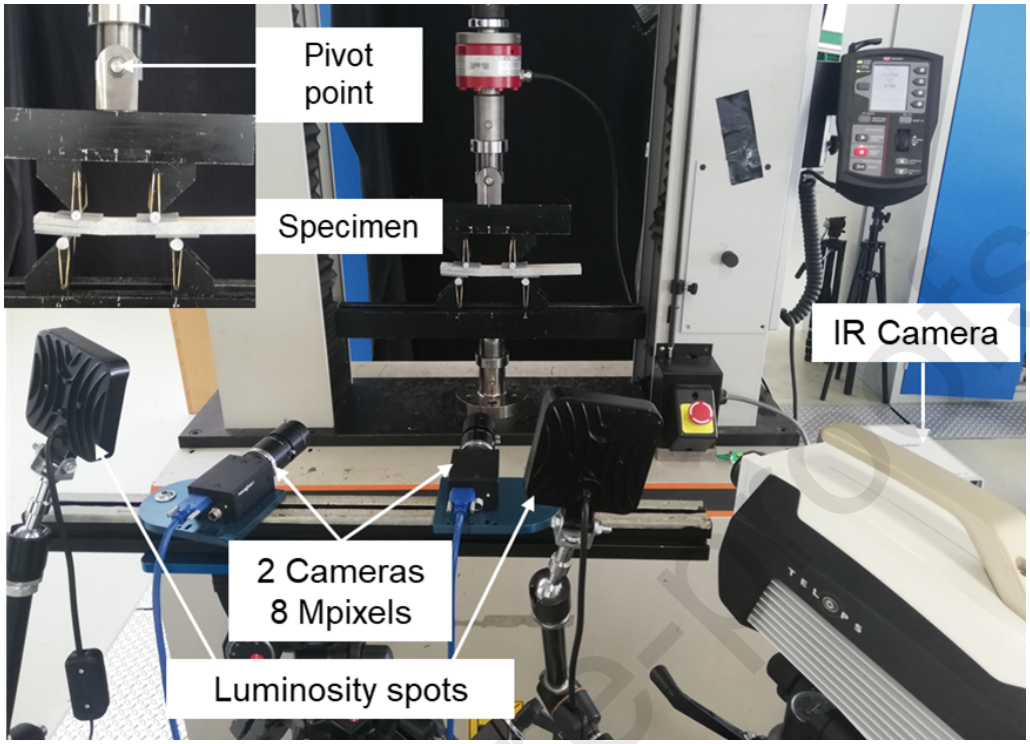

Figure 3. Experimental set-up of the 4ENF test.

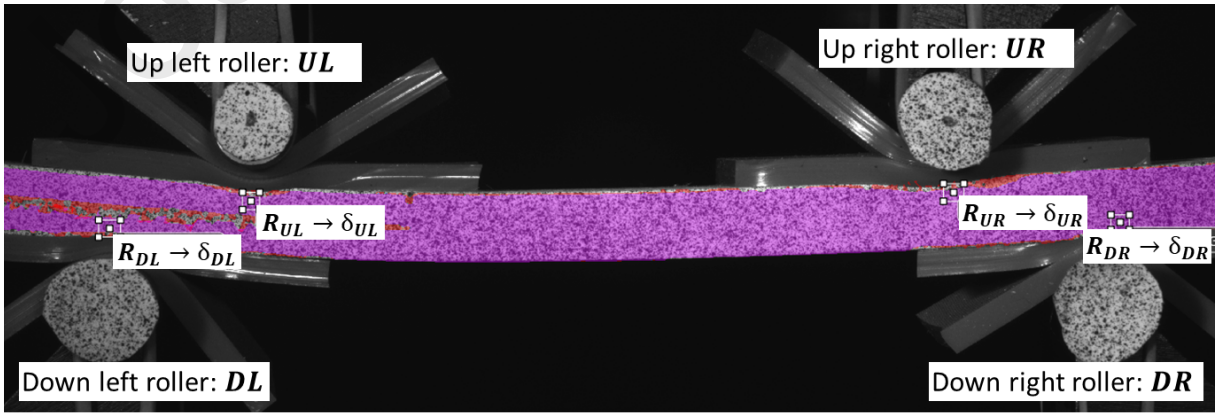

Figure 4. Calculation of the vertical displacement of the specimen with VIC-3D® software.

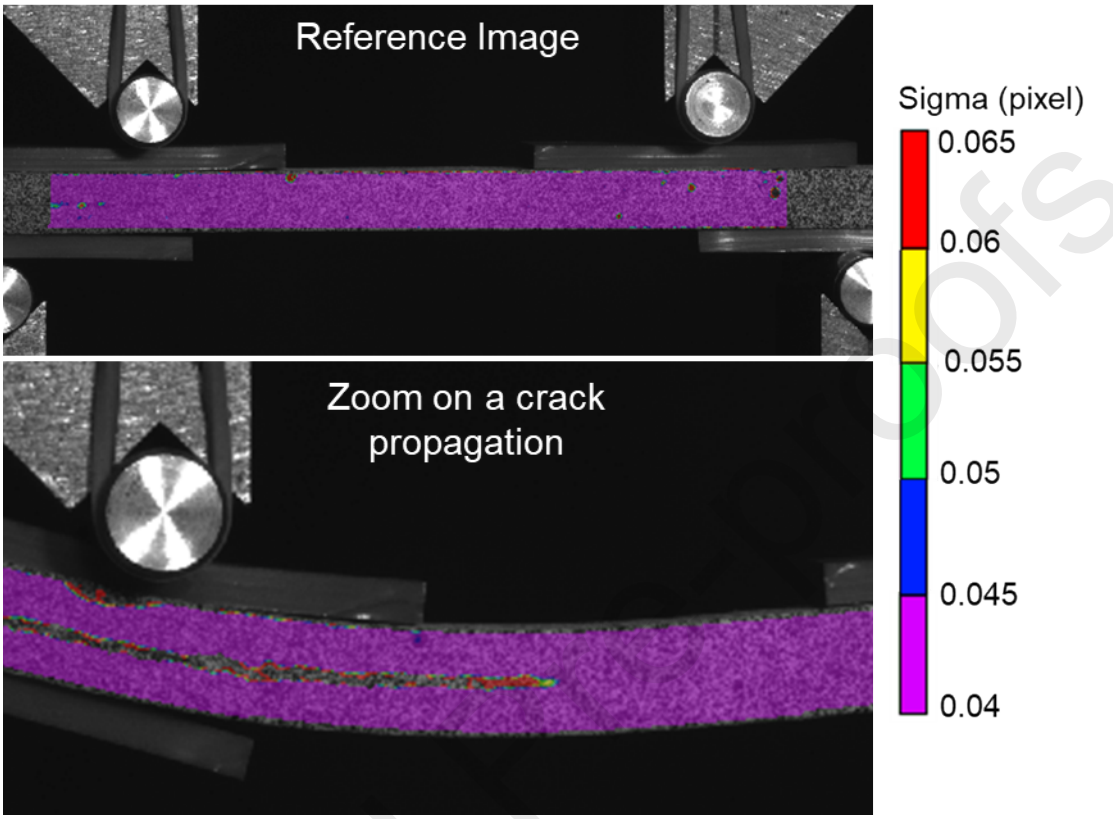

Figure 5. Crack tip monitoring using VIC-3D® software.

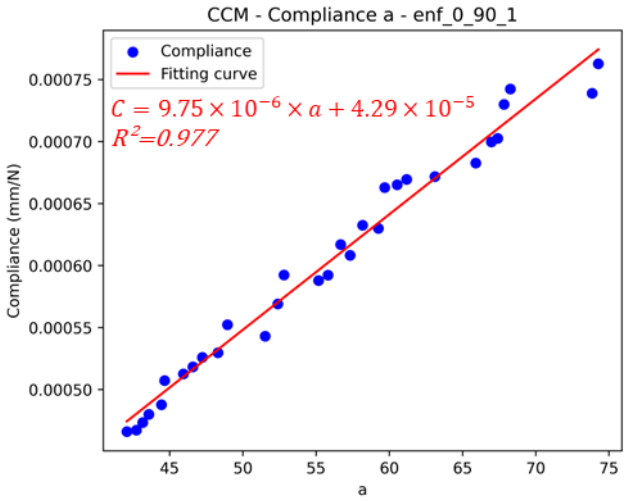

Figure 6. Example of the evolution of the specimen compliance as a function of the crack length.

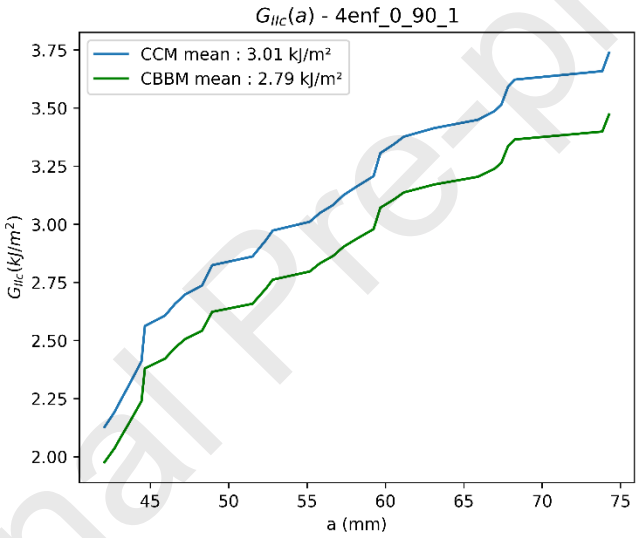

Figure 7. Example of R-curves obtained with CCM and CBBM methods.

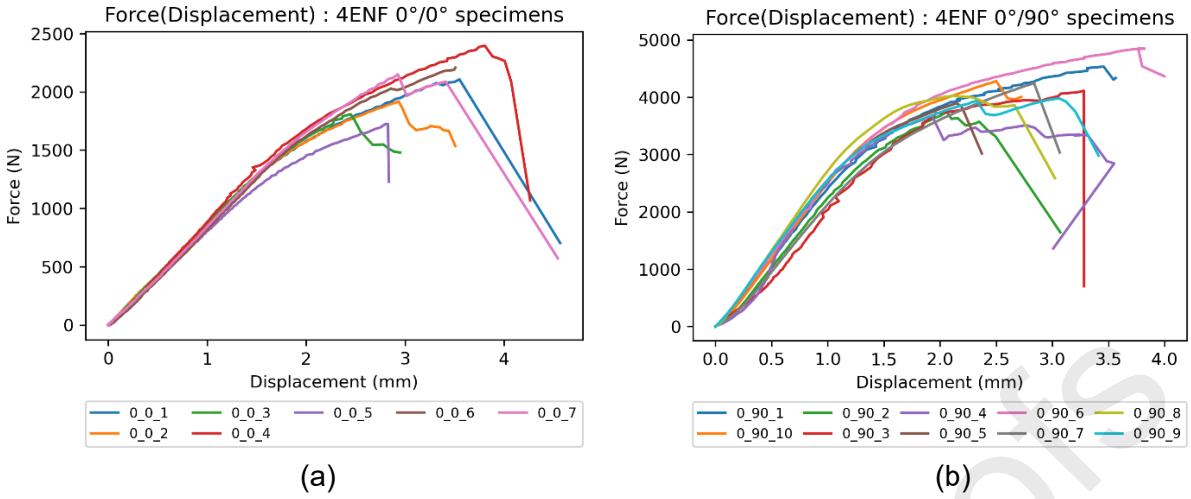

Figure 8. Evolution of the force with the displacement for (a) 0°/0° and (b) 0°/90° specimens.

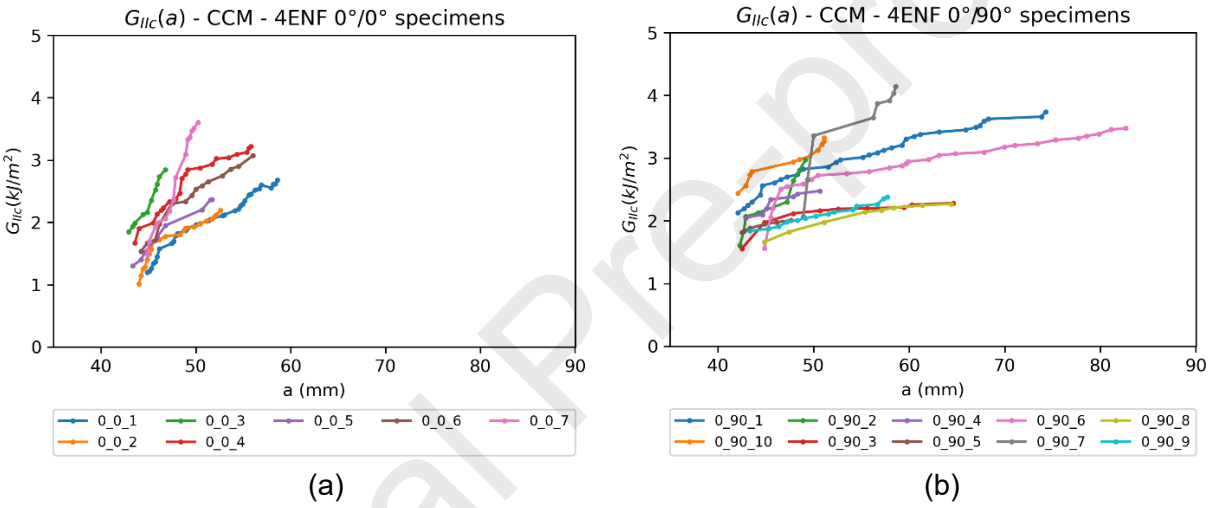

Figure 9. R-curves for (a) 0°/0° and (b) 0°/90° specimens obtained with Compliance Calibration Method.

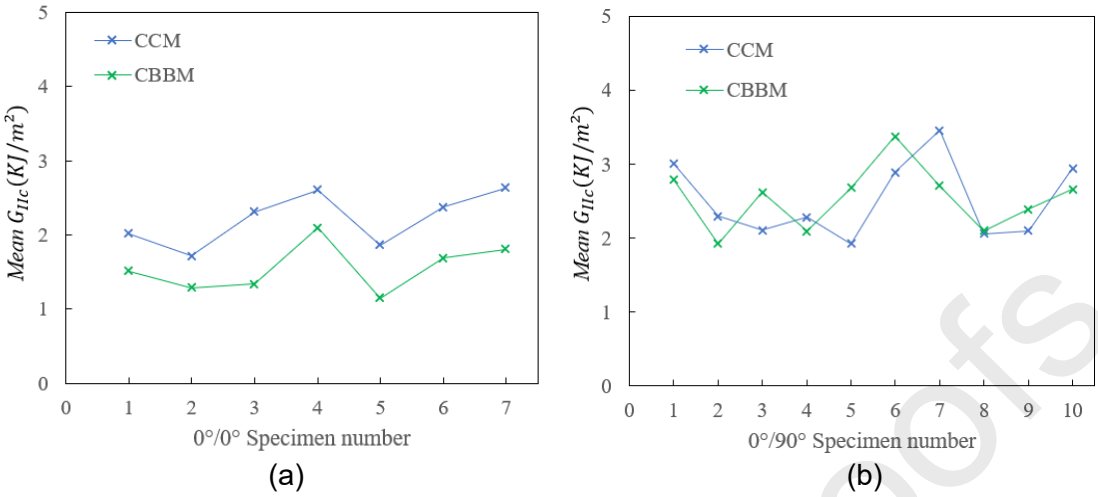

Figure 10. Mean values of G_{IIc} obtained with CCM and CBBM for (a) 0°/0° and (b) 0°/90° specimens.

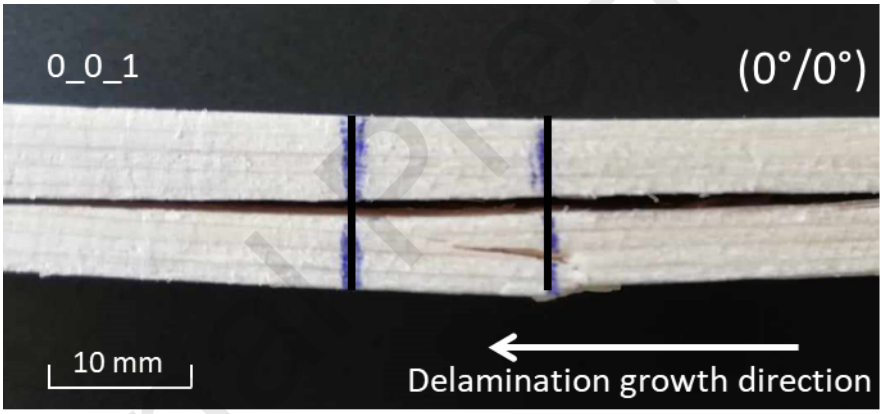

Figure 11. Side view of the delamination growth path in 0°/0° interface.

Figure 12. Side view of the delamination growth path in 0°/90° interface.

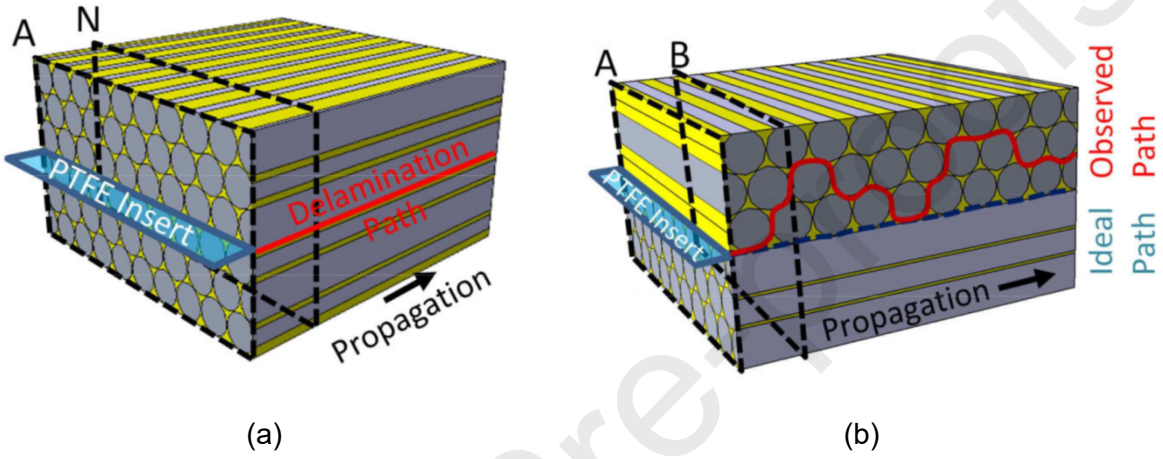

Figure 13. Delamination path for (a) 0°/0° and (b) 0°/90° specimens [35,36].

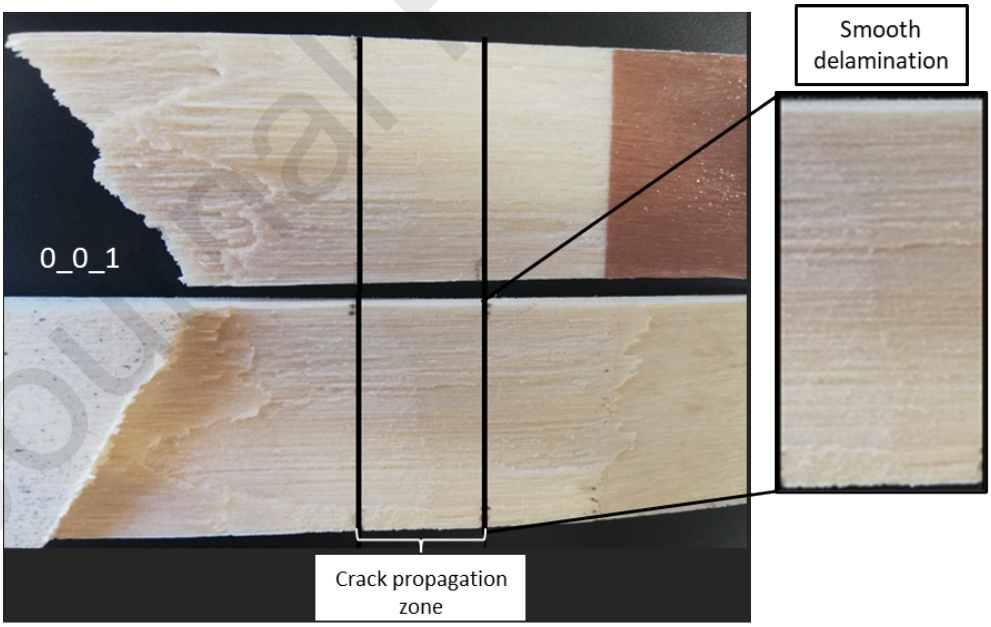

Figure 14. Fracture surfaces of a specimen with a 0°/0° interface.

Figure 15. Fracture surfaces of a specimen with a 0°/90° interface.

Declaration of interests

☒ The authors declare that they have no known competing financial interests or personal relationships that could have appeared to influence the work reported in this paper.

☐ The authors declare the following financial interests/personal relationships which may be considered as potential competing interests: